Identifying Dominant Recombination Mechanisms in Perovskite Solar Cells by Measuring the Transient Ideality Factor

Phil Calado,[1,*] Dan Burkitt,[2] Jizhong Yao,[1] Joel Troughton,[2] Trystan M. Watson,[2] Matt J. Carnie,[2] Andrew M. Telford,[1] Brian C. O'Regan,[3] Jenny Nelson,[1] and Piers R.F. Barnes[1,†]

[1]*Department of Physics, Blackett Laboratory, Imperial College London, SW7 2AZ London, UK*
[2]*SPECIFIC-IKC, College of Engineering, Swansea University, Fabian Way,Swansea SA1 8EN*
[3]*Sunlight Scientific, Berkeley, California, USA*

The light ideality factor determined by measuring the open-circuit voltage (V_{OC}) as a function of light intensity is often used to identify the dominant recombination mechanism in solar cells. Applying this "Suns-V_{OC}" technique to perovskite cells is problematic since the V_{OC} evolves with time in a way that depends on the previously applied bias (V_{pre}), bias light intensity, device architecture and processing route. Here, we show that the dominant recombination mechanism in two structurally similar $CH_3NH_3PbI_3$ devices containing either mesoporous Al_2O_3 or TiO_2 layers can be identified from the signature of the transient ideality factor following application of a forward bias, V_{pre}, to the device in the dark. The transient ideality factor is measured by monitoring the evolution of V_{OC} as a function of time at different light intensities. The initial values of ideality found using this technique are consistent with estimates of the ideality factor obtained from measurements of photoluminescence vs light intensity and electroluminescence vs current density. Time-dependent simulations of the measurement on modeled devices, which include the effects of mobile ionic charge, reveal that this initial value can be correlated to an existing zero-dimensional model while steady-state values must be analyzed taking into account the homogeneity of carrier populations throughout the absorber layer. The analysis shows that Shockley-Read-Hall (SRH) recombination through deep traps at the charge-collection interfaces is dominant in both architectures of measured device. Using transient photovoltage measurements directly following illumination on bifacial devices, we further show that the perovskite–electron-transport-layer interface extends throughout the mesoporous TiO_2 layer, consistent with a transient ideality signature corresponding to SRH recombination in the bulk of the film. This method will be useful for identifying performance bottlenecks in alternative variants of perovskite and other mixed ionic-electronic conducting absorber-based solar cells.

I. INTRODUCTION

Identifying the dominant recombination mechanisms in hybrid perovskite solar cells is necessary to rationally optimize device architectures for performance and stability. The "light" ideality factor, n_{id} (also known as the "quality factor"), determined from the open-circuit voltage (V_{OC}) dependence on light intensity (Suns-V_{OC}), has classically been employed as a means to identify the dominant recombination mechanism in silicon and organic absorber solar cells [1–3]. Applying this technique to perovskite devices is problematic, however, since mobile ions modulate recombination and injection of electronic carriers at interfaces [4–7], inducing slow transient changes in the V_{OC} that depend on light and voltage-bias device preconditioning [8]. This same process is responsible for the infamous current-voltage (J-V) hysteresis and changes in dark J-V ideality between forward and reverse scans in many perovskite devices [4,6,8–12]. Accordingly, for devices with hysteresis, light ideality factors depend on the time at which the V_{OC} is evaluated after illuminating the device as well as the state of the cell prior to illumination. Different approaches have been used in an attempt to circumvent this problem: Pockett *et al.* measured V_{OC} values only after devices had reached steady state [13]. However, a number of devices in their study showed difficult-to-rationalize values of ideality factor ($n_{id} > 5$). Tress *et al.* conducted light intensity scanning sweeps in both increasing and

_____
*p.calado13@imperial.ac.uk
†piers.barnes@imperial.ac.uk

decreasing directions and took the V_{OC} value after 3 s as a compromise between stabilization of the V_{OC} and irreversible degradation of devices [14]. Photoluminescence (PL) of the perovskite absorber layer has also been shown to evolve on the same timescale as changes in the V_{OC} and has been linked to ion migration [15,16]: ideality factor measurements on perovskite monolayers and heterojunctions using PL quantum efficiency have also been made under steady-state conditions [17]. To date, however, both a justification for interpreting the steady-state ideality factor using established quasi-zero-dimensional models and a detailed understanding of the time-dependent ideality factor in perovskite solar cells remain elusive.

In this study, we present a method for determining the transient ideality factor, $n_{id}(t)$, of a device as it evolves from an initial state, defined by a voltage preconditioning protocol in the dark, toward a steady-state value after illumination. The measurement, made by monitoring the evolution of V_{OC} for different light intensities, (which we will refer to as a "transient Suns-V_{OC}" measurement), is presented for two different device architectures, which contain either a mesoporous TiO_2 or Al_2O_3 interlayer deposited on a compact layer of TiO_2. While a mesoporous TiO_2 layer is expected to contribute to electron collection and possibly recombination, the electrically insulating nature of mesoporous Al_2O_3 is expected to block electron injection from the perovskite. Comparing the two architectures thus provides a means to control the details of possible recombination mechanisms. To cross-check the Transient Suns-V_{OC} measurement, we also present corresponding instantaneous ideality factor measurements determined from transient electroluminescence (EL) vs current density (J-EL) and PL vs light intensity (Suns-PL) where devices have similarly been preconditioned using an electrical bias in the dark. In addition, transient photovoltage measurements superimposed on the evolving V_{OC} are used to probe the behavior of charge carriers and the electric field near the interfaces. In order to interpret the experimental findings, we perform drift-diffusion device simulations describing the time-dependent evolution of the free-electron, hole, and ionic-defect concentration profiles using our home-built open-source simulation tool, Driftfusion [8,18]. The results show that devices with different recombination schemes exhibit characteristic $n_{id}(t)$ "signatures," determined by the change in electron and hole population overlap at recombination sites and modulated by the distribution of mobile ionic charges. Following forward bias, the initial and final values of the $n_{id}(t)$ can be related to an established quasi-zero-dimensional model while steady-state values must be analyzed taking into account the homogeneity of carrier populations throughout the absorber layer. These insights enable the dominant recombination mechanism to be inferred in the measured devices and resolve a long-standing contradiction whereby devices suspected of being dominated by surface

recombination have shown stabilized ideality factors of approximately 2 [14,17,19,20].

II. BACKGROUND

A. Measuring ideality factors in solar cells

The ideality factor, n_{id}, describes how the quasi-Fermi-level (QFL) separation, ΔE_F, at the terminals of a diode relate to the recombination flux density, U. In a zero-dimensional picture, it can be defined as

$$n_{id} = \frac{q}{k_B T}\frac{d\Delta E_F}{d\,\ln(U)},\tag{1}$$

where q is the elementary charge, k_B is Boltzmann's constant, and T is the device temperature (see Appendix A for the full derivation). For diodes, n_{id} is traditionally estimated from the variation of applied voltage (a measure of ΔE_F) with injected current density J (a measure of U). This approach, however, is prone to errors owing to parasitic resistances. In solar cells, n_{id} is most readily estimated from the variation of open-circuit voltage, V_{OC}, with incident photon-flux density, ϕ, given that recombination flux density is proportional to incident photon-flux density at open circuit [21,22]

$$n_{id} = \frac{q}{k_B T}\frac{dV_{OC}}{d\,\ln(\phi)}.\tag{2}$$

The relationship can also be probed using EL or PL as a direct probe of quasi-Fermi-level separation, given the exponential dependence of radiative recombination flux ϕ_{rad} on ΔE_F,

$$\phi_{rad} \propto \exp\left(\frac{\Delta E_F}{k_B T}\right).\tag{3}$$

To derive n_{id} from EL flux ϕ_{EL}, we use the injected current density J as a probe of recombination flux such that

$$n_{id} = \frac{d\,\ln(q\phi_{EL})}{d\,\ln(J)}.\tag{4}$$

To derive n_{id} from steady-state PL flux density ϕ_{PL}, we use the incident light intensity ϕ as a relative measure of total recombination flux density,

$$n_{id} = \frac{d\,\ln(\phi_{PL})}{d\,\ln(\phi)}.\tag{5}$$

A combination of two or more of these metrics can be useful to robustly probe the underlying relationship between Fermi level separation and recombination flux.

B. Ideality and recombination

Ideality factors are typically related to recombination mechanisms and their associated reaction orders using a quasi-zero-dimensional model. First, a relationship between the QFL splitting, ΔE_F, and free electron (or hole) carrier density n (or p) is defined such that

$$\Delta E_F = k_B T \ln\left(\frac{np}{n_i^2}\right) = k_B T \ln\left(\frac{n^\beta}{n_i^2}\right) + \text{const}, \quad (6)$$

where n_i is the equilibrium charge carrier density and β is a parameter defining the relationship between the carrier density and the perturbation of the QFLs from equilibrium E_{F0}. This parameter is critical to understanding the ideality factors measured in perovskite solar cells owing to the influence of electron and hole distributions by mobile ions. If $n \approx p$, then $np \to n^2$ and $\beta \to 2$. In this case, ΔE_F is split equally between the individual electron (E_{Fn}) and hole (E_{Fp}) QFLs [Fig. 1(a)].

Where a majority carrier type exists, $\beta \to 1$. This can be shown by expressing the carrier concentrations in terms of their change from equilibrium values (n_0 and p_0) such that $n = \Delta n + n_0$ and $p = \Delta p + p_0$. If $p_0 \gg \Delta p = \Delta n \gg n_0$, then the charge-density ratio in the logarithm of Eq. (6) can be written as

$$\frac{np}{n_i^2} = \frac{(n_0 + \Delta n)(p_0 + \Delta p)}{n_i^2} \approx \frac{np_0}{n_i^2}. \quad (7)$$

In this case, it is apparent that ΔE_F will be almost exclusively influenced by the changes in the minority carrier, n. Under the assumption that a single recombination reaction order, γ, dominates recombination in the device such that $U = kn^\gamma$ (where k is the order-dependent recombination-rate coefficient), n_{id} can be expressed as [22]

$$n_{id} = \frac{\beta}{\gamma}. \quad (8)$$

Table I summarizes these quantities for different recombination mechanisms, trap energies, and relative carrier-population overlap cases. The derivations of the reaction

TABLE I. The derivation of the different values of γ are given in Appendix B. Note that in the case of shallow traps, the values of β, γ, and n_{id} tend toward those for band-to-band recombination.

Recombination mechanism	Trap energy	Carrier overlap	β	γ	n_{id}
Band-to-band	NA	$n \gg p$	1	1	1
Band-to-band	NA	$n = p$	2	2	1
SRH	Shallow	$n \gg p$	1	1[a]	1[a]
SRH	Shallow	$n = p$	2	2	1
SRH	Midgap	$n \gg p$	1	1	1
SRH	Midgap	$n = p$	2	1	2

[a]$\gamma = 1$ (and thus $n_{id} = 1$) in this situation only if n is held approximately constant (for example, by a contact). SRH denotes Shockley-Read-Hall recombination.

orders corresponding to band-to-band recombination or trap-mediated Shockley-Read-Hall (SRH) [23] recombination via different trap depths are given in Appendix B. It is apparent from Table I that in the limiting cases, γ and β often cancel, resulting in an ideality of $n_{id} = 1$. SRH recombiantion via midgap trap energies is the only mechanism listed that results in a value of $n_{id} = 2$. A change in ideality as a function of time would indicate, therefore, that there has either been a shift in the dominant recombination reaction order (for example, from SRH to band-to-band dominated) or a change in the charge-density dependence of the QFL splitting as defined by the parameter β.

In thin-film solar cells, trap-assisted nonradiative recombination via defect states in the band gap is of high importance since the greatest proportion of carriers are often lost in this way. Furthemore, nonradiative recombination can be mitigated via passivation of defects, particularly at grain boundaries and interfaces [24,25]. In p-i-n structured devices with a built-in electric field, the overlap in the populations of electrons and holes at the interfaces is likely to be small, and hence idealities close to 1 are often correlated with interfacial recombination (recombination at the intrinsic-doped layer interfaces), while idealities close to 2 are identified with bulk recombination via traps (see Table I). In organic solar cells, experimental values
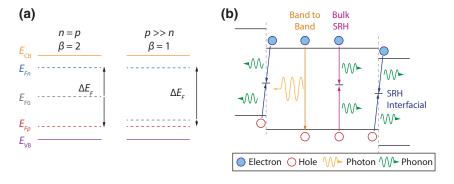

FIG. 1. Schematics of idealized QFL splitting and fundamental recombination mechanisms in perovskite solar cells. (a) Schematic of idealized quasi-Fermi-level splitting ΔE_F in a zero-dimensional material. Where $n = p$, the Fermi levels split with equal magnitude from equilibrium E_{F0} under bias. Where one carrier is in excess ($p \gg n$ is shown), the shift in the minority carrier Fermi energy dominates the change in ΔE_F. (b) Schematic illustrating different possible recombination pathways within a device.

between 1 and 2 have frequently been observed, suggesting a range of behaviors from interfacial to bulk recombination [21,26]. Idealities greater than 2 have previously been attributed to a tail of states in the band gap [27] or nonlinear shunt resistance [28]. Kirchartz *et al.* showed, however, that these processes are unnecessary to reproduce unusually high idealities in thin devices where the distribution of the carrier-population overlap is highly dependent on the device thickness and magnitude of the carrier densities [22].

Having reviewed the theoretical origins of the ideality factor, we now examine both measurements and simulations of time-dependent ideality factors in perovskite solar cells with multiple architectures and simulated recombination schemes. In particular, we focus on the influence of mobile ionic charge on localized electron and hole population overlaps, and how this alters the measured ideality factor with time.

III. METHODS

A. Devices

Measurements are performed on devices with two different architectures [device stack shown in Fig. 2(a)]:

(1) Flourine-doped tin oxide (FTO)(400 nm)/compact-TiO_2(50 nm)/mp-Al_2O_3 (250 nm)/$CH_3NH_3PbI_3$(200 nm)/Spiro-OMeTAD(200 nm)/Au(100 nm) as described in Ref. [29], which we will refer to as mesoporous Al_2O_3 (mp-Al_2O_3).

(2) FTO(400 nm)/compact-TiO_2(50 nm)/mp-TiO_2(250 nm)/$CH_3NH_3PbI_3$(200 nm)/Spiro-OMeTAD(200 nm)/Au (100 nm) as described in Ref. [30], which we will refer to as mesoporous TiO_2 (mp-TiO_2).

This allows comparison of recombination in a device containing a planar electron-transporting-material–perovskite interface with one in which the interface is likely to be extended.

B. Transient Suns-V_{OC} measurement

The history-dependent nature of the open-circuit voltage in perovskite devices requires an adaptation of the conventional Suns-V_{OC} method for determining the ideality factor. Figure 2(b) shows the experimental timeline for the measurement. The TRAnsient and Charge Extraction Robot (TRACER) system, described previously [31], is used to precondition the measured cell for a set time (typically 100 s) at a specified prebias voltage, V_{pre}, prior to the measurement of V_{OC} at each light intensity. The cell is then simultaneously switched (with microsecond precision) to open circuit and a continuous light intensity (with photon flux φ) generated by a bank of white light-emitting diodes is switched on. The evolution of $V_{OC}(t)$ is then recorded using a National Instruments USB-6251 data-acquisition card where t is the time after illumination. This procedure is sequentially repeated for each light intensity used in the measurement from low to high intensity. The transient ideality factor, $n_{id}(t)$, of the solar cell for a given precondition is evaluated from the fit to the slope of the $V_{OC}(t)$ against $\ln(\varphi)$ [Eq. (2)] in the range $\varphi = 0.2$–2 sun equivalents (calibrated using photocurrent matching of a Si photodiode generated by a solar simulator) determined at different delay times t.

C. *J*-EL measurement

EL is measured using a Shamrock 303 spectrograph combined with an InGaAs array detector cooled to –90 °C. Before measurement of EL at each injection-current density, the device is preconditioned at a voltage, V_{pre}, as described above for the Suns-V_{OC} measurements. After this poling step, the device is set to a constant injection current level ranging between $J = 1.25$ mA cm^{-2} and $J = 1250$ mA cm^{-2}. A pair of optical lenses are used to focus the resulting EL signal, allowing sampling at time intervals of between 0.02 s and 0.1 s. The EL signals are normalized relative to the value at $t = 1$ s. The relative emission flux for each injection current is
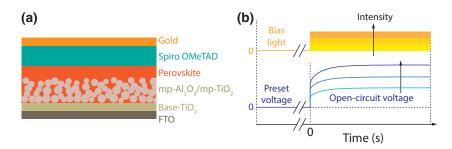

FIG. 2.   Device architecture and transient Suns-V_{OC} experimental timeline. (a) Device stack: the mesoporous layer can be either Al_2O_3 or TiO_2. (b) Transient Suns-V_{OC} experimental timeline: the cell is preconditioned in the dark at a preset voltage V_{pre} for >60 s. At $t = 0$, the bias light is switched on and the cell is simultaneously switched to open circuit. The V_{OC} is subsequently measured for >30 s. The protocol is cycled at increasing bias light intensity and the ideality factor as a function of time is calculated.

subsequently determined by integration over the whole spectrum.

D. Suns-PL measurement

PL from perovskite devices is measured with the same spectrograph and detector system as the EL setup described above. A 473-nm-diode laser is used as the excitation source, and a set of neutral density filters are applied to adjust the laser intensity. Prior to each measurement, the devices are preconditioned at V_{pre} in the dark (as described for the Suns-V_{OC} and EL-J measurements). The sample is then illuminated and the integrated PL signal is recorded with a sampling interval of 0.1 s.

E. Transient photovoltage measurements

To probe the direction of charge transport within different regions of bifacial devices, we use the TRansient Of The TRansient Photovoltage (TROTTR) technique previously introduced in Ref. [8], using a 488-nm laser excitation source superimposed on the white LED bias light. The measurement is similar to the Transient Suns-V_{OC} measurement, performed at 1-sun equivalent intensity, with the superposition of short (0.5–10 μs) 488-nm laser pulses at periodic intervals (1 s) throughout the background illumination stage to induce small perturbation photovoltage transients ΔV. The experimental timeline and experimental setup are given in Fig. S1 within the Supplemental Material [32] and Fig. 8 within Appendix G, respectively, for quick reference. The relatively short penetration depth of the laser results in charge carriers generated close to either electrode, depending on the chosen illumination side. A negative ΔV indicates the presence of a reverse electric field in the region of the active layer probed by the excitation pulse.

F. Device simulation

Our home-built PSC simulation tool Driftfusion [18] based on MATLAB's pdepe solver is used to solve for electron, hole, and mobile ion densities, and the electrostatic potential as a function of position and time in a p-i-n device structure. Here, a mirrored-cell approach with open-circuit ($J = 0$) boundary conditions is used to directly solve for the open-circuit voltage as a function of time [8]. Prior to solving with illumination, the equilibrium or quasiequilbrium solution for the cell in the dark with an applied voltage of V_{pre} is calculated to give the initial condition for the subsequent $V_{OC}(t)$ solutions. For simplicity, a uniform generation profile is used during the V_{OC} simulations and solutions are calculated for nine different constant light intensities ranging from 0.1 to 25.6-sun equivalents (where 1-sun equivalent is set to be a uniform generation rate of 2.5×10^{21} cm^{-3} s^{-1} throughout the 400-nm thickness of the intrinsic absorber layer).

A single positive mobile ionic-defect species with an initial uniform concentration of 10^{19} cm^{-3} is used in the perovskite absorber layer based on a value of 2×10^{19} cm^{-3} Shottky defects obtained from quantum mechanical calculations by Walsh *et al.* [33]. Here, the mobile defects simulate iodide vacancies, which, according to multiple calculations [34–38], are expected to have the lowest activation energy to site hopping. Densityfunctional theory calculations suggest that the iodidevacancy-defect energy levels lie outside of the band gap (or at the conduction-band edge) [39,40], and as such, these defects would not be expected to act as recombination centers. A uniform, static negative charge density of 10^{19} cm^{-3} is used to simulate a slower moving counter ion.

Low rates of second-order band-to-band recombination ($U_{BTB} \propto np$) are implemented in all layers in all recombination schemes, whereas SRH recombination (U_{SRH}) is used in different locations of the device dependent on the scheme. Table II shows the five different recombination schemes simulated for the study. The parameters used and a more complete description of the model are given in Appendix C and Appendix D, and Ref. [8]. The MATLAB code is freely available (see [41]).

Shallow and deep traps at interfaces and in the bulk are independently studied. The recombination coefficients are adjusted dependent on the trap energy to yield V_{OC} values approximately similar to those observed experimentally. For the shallow trap schemes, the trap energies are set to be in the band gap, 0.2 eV away from the conduction and valence-bands in the n and p-type layers, respectively. While symmetrical trap distributions such as this are highly improbable in reality, this approach enables the study of location-dependent recombination in isolation from asymmetric electron and hole recombination rates.

The simulated solutions for $V_{OC}(t)$ determined for the different photon fluxes are used to evaluate $n_{id}(t)$ from the slope of V_{OC} vs the logarithm of φ. Since this slope varies somewhat over the range of φ, in particular with low V_{pre}

TABLE II. Recombination mechanisms simulated in the study. The modeling parameters for the each scheme are given in Appendix D. Shallow traps are set to be in the band gap and 0.2 eV away from the conduction and valence-bands in the n and p-type layers, respectively. Midgap traps are defined to be in the center of the 1.6-eV band gap.

Scheme number	Dominant recombination mechanism	Trap energy
1	Band-to-band only	NA
2	Interface SRH	Shallow
3	Interface SRH	Midband gap
4	Bulk SRH	Shallow
5	Bulk SRH	Midband gap

values, the average value is quoted in this study (Fig. S2 within the Supplemental Material [32]).

The simulations presented here are not intended as a highly accurate representation of the measured systems, but rather as a means to gain insight into the principle device physics of solar cells with mixed ionic-electronic conducting absorber layers.

IV. RESULTS AND DISCUSSION

A. The evolution of V_{OC} with light intensity and preconditioning bias

Examples of the measured evolution for a mp-Al$_2$O$_3$ cell of the following illumination at different constant light intensities are shown in Figs. 3(a) and 3(b) preconditioned
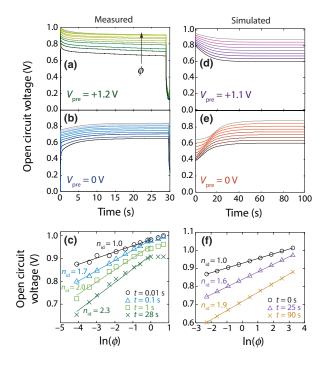
FIG. 3. Temporal evolution of the open-circuit voltage and ideality factor in measured and simulated devices. Examples of the evolution of measured V_{OC} for different incident photon fluxes ($\varphi = 0.2$–2 sun equivalents) with time following dark preconditioning with (a) $V_{pre} = 1.2$ V and (b) $V_{pre} = 0$ V for a mp-Al$_2$O$_3$ cell. (c) The measured V_{OC} plotted against incident photon flux, φ, at different delay times following illumination for the $V_{pre} = 1.2$ V case shown in (a). The ideality factor shows an increase in time. (d) The simulated evolution of the V_{OC} for different incident photon fluxes ($\varphi = 0.1$–25.6 sun equivalents) from a $V_{pre} = 1.1$ V dark equilibrium solution and (e) from a $V_{pre} = 0$ V dark equilibrium solution. For both preconditioning cases shown in the example, recombination scheme 3 is used in the simulation (Table II, band-to-band in bulk, and interfacial SRH recombination via midgap states). (f) Simulated V_{OC} vs incident photon flux, φ, at different delay times following illumination for the dark $V_{pre} = 1.1$ V initial conditions case shown in (d) also shows an increase in ideality factor with time.

at $V_{pre} = 1.2$ V and $V_{pre} = 0$ V, respectively, in the dark. Following $V_{pre} = 1.2$ V, the V_{OC} gradually decays over the course of 30 s from an initially higher value toward a steady-state value for each light intensity. In contrast, following $V_{pre} = 0$ V, the V_{OC} rises toward a steady-state value. The V_{OC} transients for the mp-TiO$_2$ device are qualitatively similar (Fig. S3 within the Supplemental Material [32]). Figure 3(c) shows that the slope of V_{OC} plotted against the logarithm of photon-flux density increases with time after illumination for the $V_{pre} = 1.2$ V case. At the beginning of the measurement ($t = 10$ ms), the ideality factor is equal to 1 then increases to a value of 2.3 after 28 s of stabilization at open circuit.

Figures 3(d) and 3(e) show examples of the evolution of calculated V_{OC} as a function of time and light intensity for two initial conditions corresponding to quasiequilibrium at $V_{pre} = 1.1$ V and equilibrium at $V_{pre} = 0$ V for a simulated device dominated by interfacial SRH recombination via midgap states (scheme 3 in Table II). The results reproduce the majority of features recorded in the experimental results [Figs. 3(a) and 3(b)] and are similarly used to find n_{id} following different illumination times [Fig. 3(f)]. Remarkably, the simulated ideality factor following forward bias also changes from an initial value of 1 to a stabilized value of close to 2.

We have previously discussed the mechanism underlying the evolution of V_{OC} at 1-sun equivalent intensity following different preconditioning biases in considerable detail [8]. The gradual change in V_{OC} often observed in perovskite cells can be explained by a slow redistribution of ionic charge from an initial state toward a new dynamic equilibrium at open circuit in the light. The initial state of the ion distribution is defined by the internal potential resulting from the combination of the built-in and preconditioning voltages: estimates of intrinsic defect densities $>10^{19}$ cm^{-3} suggest that typical field strengths in thin-film perovskite devices will be entirely screened by ionic charge, with Debye lengths of less than 10 nm [10,33]. Upon illumination at open circuit, the development of a photovoltage and associated change in the electric field distribution can result in either enhanced segregation of photogenerated electrons and holes toward the charge-collecting contacts (following positive V_{pre} close to the open-circuit potential) or segregation of electronic carriers toward the opposite contacts (following zero or negative V_{pre}), as shown in the example device simulations in Figs. 4(a) and 4(b). If these ion-distribution effects are combined with significant interfacial recombination, the V_{OC} either slowly increases or decreases from its initial value as the mobile ionic charge moves to a new equilibrium distribution, modulating the electronic carrier concentrations at the interfaces in its wake. Once a steady state is established, the internal electric field within the perovskite layer is again screened by an accumulation of ionic charge and a new V_{OC} value is reached [Fig. 4(c)]. The
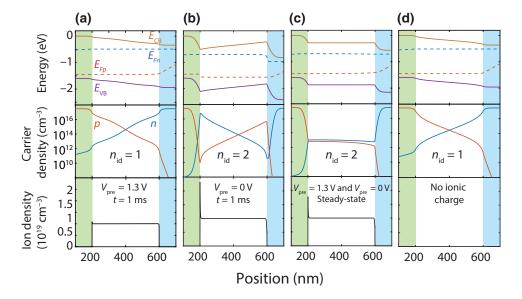
FIG. 4. Example energy-level diagrams and charge-density profiles during the open-circuit-voltage transient simulation. Energy-level diagrams (E_{CB} and E_{VB} are the conduction and valence-band energies, while E_{Fn} and E_{Fp} are the electron and hole quasi-Fermi-levels, respectively), electron (n), hole (p), and mobile ion densities after simultaneously illuminating and switching to open circuit with $\varphi = 1.6$ sun equivalent for a device preconditioned with (a) $V_{\mathrm{pre}} = 1.3$ V in the dark at $t = 1$ ms following illumination, (b) $V_{\mathrm{pre}} = 0$ V in the dark at $t = 1$ ms following illumination, and (c) at steady state ($t = 100$ s) for both preconditions at open circuit. (d) A device with the same parameter set without mobile ions. Recombination scheme 3 (Table II) is used in the simulation results shown. The green and blue shaded regions indicate the respective p and n-type regions of the device.

hysteresis observed in the *J-V* scans and V_{OC} transients of the devices measured in this study (Fig. S4 within the Supplemental Material [32] and Fig. 3, respectively) provide strong evidence for ion-modulated recombination in the measured devices [4,5,7]. The rate of ionic redistribution will depend on the ionic conductivity, contact capacitance, light intensity, and magnitude of the preconditioning bias. The details of how this redistribution influences the evolution of the transient ideality factor will, in turn, depend on the details of the recombination processes in the device and are discussed below.

B. Transient ideality factors

Figure 5 shows the evolution of $n_{\mathrm{id}}(t)$ for the two different types of device following dark preconditioning at $V_{\mathrm{pre}} = 1.2$ V (mp-Al$_2$O$_3$ device) and $V_{\mathrm{pre}} = 1.0$ V (mp-TiO$_2$ device) at bias light intensities of 0.2–2 sun equivalents. For the mp-Al$_2$O$_3$ cell (green curve, circle markers), following $V_{\mathrm{pre}} = 1.2$ V, the ideality starts at $n_{\mathrm{id}}(t = 0) \approx 1$ and increases to approximately 2.1 during the 30 s of the measurement. When the ideality for the same cell is evaluated following $V_{\mathrm{pre}} = 0$ V, the values of n_{id} are much higher than expected given the classical interpretation, starting at 3.7 and decreasing to approximately 1.8 (Fig. S5(a) within the Supplemental Material [32]).

The mp-TiO$_2$ cell (light blue curve, triangle markers) also shows an increase in n_{id} following $V_{\mathrm{pre}} = 1.0$ V, from 1.5 to around 2.7. The curve appears similar in shape

to that of the mp-Al$_2$O$_3$ device, but shifted with respect to the *y* axis. Following $V_{\mathrm{pre}} = 0$ V, the n_{id} again shows much higher values, starting at 3.2 and finishing at 2.6 (Fig. S5(a) within the Supplemental Material [32]). A summary of the initial and final n_{id} values for different measurement techniques and preconditioning voltages is given in Table III. For real-world applications, where solar cells are operated at the maximum-power point under solar illumination, the steady-state ideality factor following $V_{\mathrm{pre}} = 0$ V is of greatest relevance owing to day-night illumination cycling. We note that the final values measured here of $n_{\mathrm{id}} \approx 2$ are consistent with stabilized values measured in previous works for standard architecture planar devices [14,17,19,20]. This suggests that either bulk or surface recombination via deep traps is limiting the performance of devices and that further optimization of both the perovskite material and interfaces to limit nonradiative recombination pathways is possible.

We note that when the measurement protocol is applied to devices with poor degradation stability, we observe irreversible losses during the measurement that typically result in a variation in the initial value of the ideality (see Appendix F). When the measurements are applied to more stable devices, we observe repeatability in the transient ideality factor signature and are able to correlate the results with our simulations.

To interpret these experimental observations, the transient Suns-V_{OC} measurement protocol is simulated for the different recombination schemes shown in Table II,
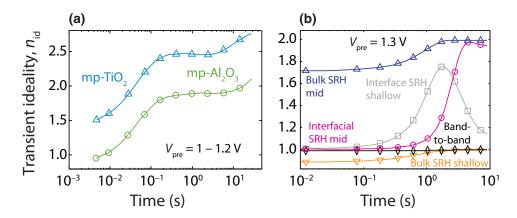
FIG. 5.   Measured and simulated evolution of the ideality factor with time following forward biasing. Measured $n_{id}(t)$ for mp-TiO$_2$ (light blue curve, triangle markers) and mp-Al$_2$O$_3$ (green curve, circle markers) cells following dark (a) $V_{pre} = 1.2$ V (mp-Al$_2$O$_3$ device), $V_{pre} = 1.0$ V (mp-TiO$_2$ device). (b) The simulated transient ideality factor, $n_{id}(t)$, derived from simulations of $V_{OC}(t)$ for different incident photon fluxes in a *p-i-n* structure starting from initial conditions simulated for dark equilibrium with $V_{pre} = 1.3$ V. The results from simulations with different dominant recombination mechanisms are shown: band-to-band recombination (black curve, diamond markers), interfacial SRH recombination via shallow traps (gray curve, square markers), interfacial SRH recombination via deep traps (pink curve, circle markers), bulk SRH recombination via shallow traps (yellow curve, inverted triangle markers), and bulk SRH recombination via deep traps (dark blue curve, triangle markers).

allowing $n_{id}(t)$ to be evaluated from the results for the two initial conditions. Remarkably, the five different recombination schemes each produce unique transient ideality signatures enabling direct identification of the dominant recombination mechanism in the simulated devices. Since the primary recombination mechanism is fixed in the simulations (Fig. S6 within the Supplemental Material [32]), and thus the reaction order γ is constant, the observed variation in n_{id} can be related to variation in β [c.f. Eq. (8)], which defines the relationship between the charge-carrier density and the perturbation of the QFLs from equilibrium. Examination of the initial [Fig. 4(a)] and final [Fig. 4(c)] simulated electron and hole profiles for scheme 3, the $V_{pre} = 1.3$ V case, reveals a change in the electron and hole population overlap in the interface regions as the ions redistribute. Initially, $n \gg p$ is at the *n*-type interface (and $p \gg n$ at the *p*-type interface), while in the final state, $n \approx p$ at both interfaces. This statement can be generalized to all recombination schemes since the energy-level diagrams and electron, hole, and ion profiles are qualitatively similar in all cases. The similarity in electronic charge-density profiles following preconditioning at $V_{pre} = 1.3$ V [Fig. 4(a)] and that of a simulated device with a built-in field and without mobile ionic charge [Fig. 4(d)] is highly significant; the preconditioning stage reduces the density of ionic charge accumulated at the interface with respect to $V_{pre} = 0$ V [Fig. 4(b)] and results in an electric field in the device at $t = 0$ s of the measurement, which drives charge carriers toward their respective transport layers. We note that this internal field would be induced by preconditioning at forward bias regardless of the strength of the built-in field. Consequently, forward biasing with an

applied potential sufficient to separate the electron and hole densities at the interfaces determines the conditions for measuring an instantaneous ideality factor, which can be interpreted using the quasi-zero-dimensional theory (outlined in the introductory theory section). The steady-state n_{id} value can only be interpreted correctly by considering the fact that $n \approx p$ ($\beta \approx 2$) throughout the active layer (see Table I). More specifically, following a sufficient forward bias, the parameter β always increases from 1 to 2 at the interfaces. In some cases, such as where SRH-surface recombination via midgap traps is dominant, the ideality is sensitive to this change (n_{id} changes from 1 to 2). In other cases, for example, where bulk recombination dominates, the ideality factor will remain largely unaffected. For surface recombination with shallow trap energies, the reaction order also changes from 1 to 2, canceling the change in β and leading to no overall change in ideality ($n_{id} = 1$ throughout). The transient ideality curve obtained after forward biasing, therefore, provides a signature for different recombination mechanisms in the device and can be correlated to the values in Table I by considering how β changes in time at positions in the device where recombination is localized.

We note that the linearity of the V_{OC} vs $\ln(\varphi)$ curves used to determine $n_{id}(t)$ is considerably greater following the forward-bias precondition relative to the zero-bias condition (see examples in Fig. S2). Combined with the discrepancy between the ideality following $V_{pre} = 0$ V for different measurement techniques discussed in Appendix E, this suggests that $n_{id}(t)$ determined following forward biasing provides a more reliable measure of the recombination mechanism. The evolution of the transient ideality factor

following $V_{\text{pre}} = 0$ V is discussed further in the caption to Fig. S5 (see Supplemental Material [32]).

C. Comparison with instantaneous idealities determined from electroluminescence and photoluminescence measurements

To cross-check the values of n_{id} experimentally measured using the transient Suns-V_{OC} method, we make further measurements of the initial value of the ideality factor $n_{\text{id}}(t \approx 0)$ following dark prebiasing using both EL vs current density measurements (J-EL) and PL vs illumination intensity measurements (Suns-PL). Figure 6 shows examples of these measurements, the results of which are summarized in Table III.

There is good agreement between the ideality values determined using the different methods following $V_{\text{pre}} > 0$. For $V_{\text{pre}} = 0$, we note discrepancies between the Suns-PL measurements and Suns-V_{OC} values in some cases, leading us to concentrate our analysis on transient ideality factors derived for $V_{\text{pre}} > 0$ (this is discussed further along with possible explanations in Appendix E). Overall, the agreement between the different techniques suggests that the concept of a transient ideality factor measured by the Suns-V_{OC} technique is related to recombination processes and not to charge storage or capacitive effects within the cell. This conclusion is further supported by recent work from our group and others [5,7] showing that modulation of interfacial recombination processes by out-of-phase ionic currents can give rise to large measured imaginary components of the impedance spectrum, previously interpreted as "giant" electronic capacitances. We note here that while it may be possible for degeneracy to occur at interfaces under specific conditions in certain architectures of devices, it is unnecessary to explain the measured apparent capacitances.

D. Assignment of recombination mechanisms to the measured devices

Different recombination mechanisms might be expected to dominate different device architectures. By comparing the experimentally measured values to simulated transient ideality curves in Fig. 5, we assign the evolution

of the measured $n_{\text{id}}(t)$ to likely dominant recombination schemes. We do not assert here that the dominant recombination mechanisms we assign to the devices will always represent the dominant recombination route for the respective architectures, since it is very likely that variation in the processing during device fabrication can lead to a number of possible recombination routes and thus device-to-device variation in $n_{\text{id}}(t)$ for cells prepared with the same architecture (discussed further in Appendix F). Rather, the approach described here presents a means to assess the most likely recombination routes for a particular device.

1. Recombination mechanism in the mesoporous Al₂O₃ cell

As discussed above, the transition in $n_{\text{id}}(t)$ from 1 to 2 for the mp-Al₂O₃ cell (Fig. 5, green curve, circle markers) is mirrored in the simulated device for which interfacial SRH recombination via midband-gap states is the dominant mechanism. This recombination scheme is also consistent with the large degree of J-V hysteresis seen in this device (Fig. S4(a) within the Supplemental Material [32]), since we and others have previously shown that a combination of mobile ionic charge and interfacial recombination are necessary to observe hysteresis [6,8,9,17,42]. While computational studies on defective $CH_3NH_3PbI_3$ crystals have not shown deep trapping states with easily accessible activation energies [39,40], the interface between $CH_3NH_3PbI_3$ and the compact TiO_2 layer is likely to contain a high density of deep interband-gap electronic states as commonly observed at the TiO_2 hole-transporting-material interface in dye-sensitized solar cells [43,44]. Furthermore, recent studies have shown that recombination rates at the hole-transport-layer interface are significantly influenced by doping [20] and that the $CH_3NH_3PbI_3$ interface with heavily lithium-doped Spiro-OMeTAD is a site of significant recombination [17].

As expected, for the simulated device with recombination scheme 3 [Figs. 3(d)–3(f), 4(a)–4(c) and 5(b)], the spatially integrated recombination fluxes in the simulated device indicate that SRH recombination at the contacts dominates at all times during the simulation [Fig. 6(d)].

TABLE III. Summary of the instantaneous and steady-state ideality factors measured for different devices using different techniques.

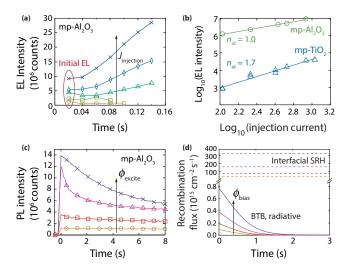| Cell architecture	Precondition voltage, V_{pre} (V)	Instantaneous ideality, $n_{\text{id}}(t \approx 0)$			1-sun equivalent J-V performance	
		Suns-V_{OC}	J-EL (0.02 s)	Suns-PL (0.01 s)	Apparent PCE (%)	V_{OC} (V)
mp-AL₂O₃	1.2	1.0	0.9	0.9	10.5	1.03
	0	3.6	...	2.0	6.7	0.94
mp-TIO₂	1.0	1.5	1.7	1.6	9.7	0.86
	0	3.2	...	1.8	7.1	0.81

PCE, Power Conversion Efficiency

FIG. 6.   Alternative measurements of the initial transient ideality factor using EL and PL. (a) Integrated electroluminescent emission flux density vs time for different injection current densities, $J = 107$, 213, 426, 533, and 853 mA cm^{-2} following the application of $V_{pre} = 1.1$ V to a mp-Al$_2$O$_3$ cell. (b) Evaluation of n_{id} for $t = 0$–0.02 s from EL emission flux density vs injection current density for the three architectures of the device. (c) Integrated photoluminescent flux density vs time for different excitation intensities following the application of $V_{pre} = 1.2$ V to a mp-Al$_2$O$_3$ cell. (d) Simulated integrated band-to-band (BTB, radiative, solid curves) and interfacial SRH recombination (dashed curves) fluxes as a function of time for a cell with recombination scheme 3 for $V_{pre} = 1.3$ V.

There is, however, a significant decay in the fraction of recombination arising from band-to-band recombination during the simulation, consistent with the reduction in PL signal with illumination time observed over a timescale of seconds in the mp-Al$_2$O$_3$ device [Figs. 6(c) and 6(d)] and previously reported in lateral perovskite devices preconditioned with similar field strengths [16]. This PL decay can be explained by an increase in nonradiative recombination at interfaces as electronic carrier densities are modulated by ion migration. This, in turn, leads to lower bulk carrier densities [consistent with the V_{OC} decays seen in Fig. 6(d)] and hence lower radiative flux. A similar (albeit opposite) mechanism could account for the increase in EL as a function of time in Fig. 6(a). Together, the transient ideality signature, J-V hysteresis, and slow timescale PL decay provide strong evidence that the mp-Al$_2$O$_3$ device is dominated by surface recombination via deep interband-gap states.

2. Recombination mechanism in the mesoporous TiO$_2$ cell

The transient ideality factor profile of the mp-TiO$_2$ [Fig. 5(a), light blue curve, triangle markers] following $V_{pre} = 1$ V shows an intermediate behavior between interfacial [Fig. 5(b), pink curve, circle markers] and bulk SRH

recombination [Fig. 5(b), dark blue curve, triangle markers] via midband-gap traps within the bulk of the active layer.

In order to further investigate the origin of the initial measured ideality value of 1.5, we probe the internal electric field by performing TROTTR on similar mp-TiO$_2$ and mp-Al$_2$O$_3$ architecture devices fabricated using a transparent conductive adhesive (TCA) top electrode [45] with a short-wavelength laser-excitation source. The absorption coefficient for CH$_3$NH$_3$PbI$_3$ at 488 nm is 1.84×10^5 cm^{-1}, giving a characteristic optical path length of 54 nm (see optical modeling in Appendix H). Thus, only electronic charge carriers generated close to the illumination-side contact are expected to contribute to transient changes in the photovoltage (ΔV).

Figure 7 shows the results of the TROTTR experiments combined with schematics of the inferred band—energy-level diagrams of the mp-TiO$_2$ and mp-Al$_2$O$_3$ devices. In both cases, the cells are preconditioned at $V_{pre} = 0$ V for 60 s prior to illumination at 1-sun equivalent intensity. Upon illumination, the configuration of ions under these conditions would be expected to initially induce a reverse field in the devices similar to that seen in the simulated device following $V_{pre} = 0$ V [Fig. 4(b)] [4,10,46]. At early times (<10 s) following illumination through the TCA side of the device, the TPV signal for the mp-TiO$_2$ shows a distinct negative deflection [Fig. 7(a), purple-pink curves]. This negative response is significantly less pronounced when the device is instead illuminated through the glass-FTO side [Fig. 7(b), purple-pink curves]. We interpret this as evidence that the inverted electric field is predominantly confined to the pure perovskite phase in the device containing mp-TiO$_2$ as shown in Fig. 7(c). In our schematic, we have approximated the mesoporous region as a homogenous medium similar to the bulk heterojunction in an organic solar cell [3,47,48]. While on the nanoscale, the details of the field are likely to be more complex, here we illustrate the average field direction in the active layer. Carriers generated close to the hole transport layer drift in the wrong direction with respect to charge collection, leading to an increased accumulation of minority charge carriers at the Spiro OMeTAD-Perovskite interface, increased recombination, an associated negative transient photovoltage (TPV) deflection and reduced signal magnitude as compared to later times in the measurement [4]. Conversely, carriers generated in the mesoporous region diffuse toward the correct contact, generating a positive signal and suggesting that, on average, the field must be low throughout the mesoporous region. After 50 s the majority of the mobile ionic charge has migrated to screen out the field and the signal becomes similarly positive independent of illumination side [Figs. 7(a) and 7(b), blue curves].

When the same experiment is repeated on the mp-Al$_2$O$_3$ device, a similar negative deflection is apparent in
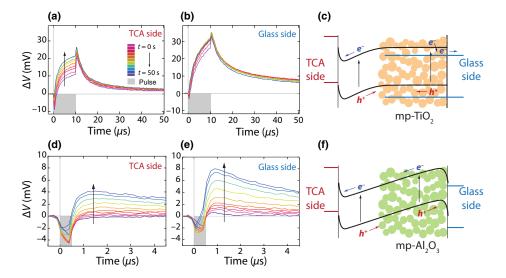
FIG. 7. Transient photovoltage measurements on bifacial devices and band-energy-level schematics for mp-TiO$_2$ and mp-Al$_2$O$_3$ architectures. Transient photovoltage ΔV measurements for following $V_{pre} = 0$ V (see the experimental timeline in Fig. S1 within the Supplemental Material [32]). The mp-TiO$_2$ device shows an initial negative deflection to ΔV when excited through (a) the TCA side by the 488-nm laser pulse. (b) The change in signal is much smaller when the device is excited through the glass side, implying an inverted electric field is localized to the TCA side as shown in (c) the band schematic. The mp-Al$_2$O$_3$ device shows similar negative initial ΔV responses when illuminated through both (d) TCA and (e) glass sides, implying the inverted field is extended into the electronically insulating mp-Al$_2$O$_3$ region as shown in (f) the device band schematic. mp-TiO$_2$ and mp-Al$_2$O$_3$ are indicated by the yellow and green shaded areas, respectively. Spiro-OMeTAD, perovskite, and TiO$_2$ conduction and bands are shown as red, black, and blue curves, respectively (energies not to scale).

the initial TPV signals independent of the illumination side [Figs. 7(d) and 7(e), purple-pink curves], suggesting that the field is extended throughout the perovskite in the mesoporous region [Fig. 7(f)]. During illumination at open circuit, the TPV signal follows a similar evolution to a more positive signal independent of the illumination side in the proceeding 50 s. The persistent negative signal during the pulse after 50 s implies a long-lived polarization in the device that could result from slower moving ionic species [49]. Following forward-bias preconditioning at $V_{pre} = 1$ V, the negative component of the signal diminishes in all cases, indicating that the strength of the inverted field at open circuit is reduced (Fig. S7 within the Supplemental Material [32]), consistent with the simulation following forward-bias preconditioning in Fig. 4(a).

Given that for the mp-TiO$_2$ device the field appears to fall predominantly in the pure perovskite phase, we propose that at the Spiro-OMeTAD interface, the carrier populations are separated ($\beta \approx 1$), while within the mesoporous region and at the c-TiO$_2$ interface, the carrier populations are approximately equal ($\beta \approx 2$) following a forward-bias precondition. The scaffold is likely to introduce deep trapping states in the region of this extended interface, leading to a reaction order of $\gamma \approx 1$. If both interfaces have similar SRH time constants, then an ideality of $1 < n_{id} < 2$ is expected: in this case, while the device might still be dominated by interfacial recombination,

the overlapping electron and hole populations ($n \approx p$) throughout the mesoporous region would result in an ideality factor greater than 1. Further work incorporating the mesoporous region into models will be required to test the above hypotheses. The reduced hysteresis in the cell's J-V curve by comparison with the mp-Al$_2$O$_3$ device (Fig. S4 within the Supplemental Material [32]) also supports the hypothesis that recombination is dominated by bulklike effects [9].

In summary, these experimental observations imply that the extended interface introduced by the mp-TiO$_2$ allows for recombination of electrons and holes via deep traps throughout the mesoporous region, which appear bulklike owing to the extended mesoporous charge-collection interface. In contrast, cells with mesoporous Al$_2$O$_3$ appear to be dominated by deep-trap recombination primarily confined to the charge collecting interfaces, and not extending through the insulating mesoporous layer.

V. CONCLUSIONS

We introduce a method to evaluate the transient ideality factor of perovskite solar cells following a voltage preconditioning period in the dark. By modeling devices using drift diffusion simulations, we correlate the transient ideality curves extracted from experimental transient Suns-V_{OC} measurements with the dominant recombination mechanism in real-world devices. This approach allows

meaningful information about the dominant recombination mechanism to be derived in the presence of mobile ionic defects. The mobile ions result in an evolving electrostatic profile throughout the thickness of a perovskite solar cell, and consequently, a time-varying V_{OC}, which hampers measurement of an ideality factor by conventional means. By preconditioning cells at a forward-bias potential sufficient to separate the charge-carrier densities at the interfaces, the cell can temporarily be set in a state that would yield a similar ideality factor to a similar device that contained no mobile ions and could thus be analyzed using an established zero-dimensional theory applied to ideality factors. The evolution of the ideality to a steady-state values is understood by taking into account the modulation of carrier-population overlap at positions of localized recombination by mobile ions.

With the aid of time-dependent device simulations, we show that the evolution of the ideality factor following different voltage preconditions can be used as a signature to identify the dominant recombination mechanism in a perovskite solar cell. We demonstrate this idea with standard perovskite device architectures incorporating mp-TiO$_2$ and mp-Al$_2$O$_3$ scaffolds. For these examples, we assign interfacial recombination via deep traps at the charge collection layer interfaces as the dominant recombination mechanism in both device types. Transient photovoltage measurements on bifacial devices indicate that, distinct from the mp-Al$_2$O$_3$ device, the electric field is predominantly confined to the pure perovskite region in the mp-TiO$_2$ architecture. The homogeneity of electron and hole populations throughout the extended mpTiO$_2$ interface results in a measured initial ideality following a forward bias of 1.5 despite interfacial recombination remaining as the dominant mechanism in the device.

We emphasize that the dominant recombination mechanism can vary between devices that were nominally prepared in the same way, an observation we attribute to small differences in the processing conditions and microstructures of the cells. We also note that our observations do not preclude the possibility that trap energy and spatial distribution in the device may be dependent on the distribution of ionic defects. Together, our findings provide additional insight on the meaningful interpretation of ideality measurements in perovskite solar cells and a valuable tool for assigning the dominant-recombination mechanism in devices.

APPENDIX A: DERIVATION OF IDEALITY FACTOR N_{id}, AS A FUNCTION OF THE CHARGE-CARRIER-DENSITY RELATIONSHIP TO FERMI-LEVEL SPLITTING β, AND THE REACTION ORDER γ

Using the Shockley diode equation, the ideality factor, n_{id} can be expressed in terms of the quasi-Fermi-level splitting ΔE_F (identical to the V_{OC} in the zero-dimensional model) and recombination rate, U, such that

$$n_{id} = \frac{q}{k_B T} \frac{d \, \Delta E_F}{d \, \ln(U)},$$

where q is the elementary charge, k_B is Boltzmann's constant, and T is the temperature.

Substituting $\Delta E_F = k_B T \ln(n^\beta / n_i^2)$ and $U = kn^\gamma$ yields

$$
\begin{aligned}
n_{id} &= \frac{q}{k_B T} \frac{d \left\{ \frac{\beta k_B T}{q} [\ln(n) - \ln(n_i^{(2-\beta)})] \right\}}{d\{\gamma [\ln(n) + \ln(k_\gamma^{(1-\gamma)})]\}} \\
&= \frac{\beta}{\gamma} \frac{d\{[\ln(n) - \ln(n_i^{(2-\beta)})]\}}{d\{[\ln(n) - \ln(n_i^{(2-\beta)})]\}}. \quad \text{(A1)}
\end{aligned}
$$

Let

$$
\begin{aligned}
x &= \ln(n), \\
b &= -\ln(n_i^{(2-\beta)}), \\
c &= \ln(k_\gamma^{(1-\gamma)}), \\
n_{id} &= \frac{\beta}{\gamma} \frac{d(x + b)}{d(x + c)}.
\end{aligned}
$$

Using the variable substitution $x = x' - c$,

$$n_{id} = \frac{\beta}{\gamma} \frac{d(x' + b - c)}{dx'} = \frac{\beta}{\gamma}.$$

APPENDIX B: DERIVATION OF REACTION ORDERS

Here, we examine how the reaction order, γ, for the general form of the equation describing the recombination rate, U, in terms of the electron concentration, n, and the reaction-order-dependent recombination rate coefficient

$$U = kn^\gamma$$

depends on the recombination mechanism and relative concentration of electrons and holes as listed in Table I of the main text.

1. Band-to-band recombination

For $n = p$, the recombination rate, U, is given by

$$U_{\mathrm{BTB}} = k_{\mathrm{BTB}} np = k_{\mathrm{BTB}} n^2,$$

where k_{BTB} is the band-to-band recombination rate constant, hence $\gamma = 2$.

For $n \gg p$, the majority carrier density can be considered as effectively constant, leading to

$$U_{\mathrm{BTB}} \propto p,$$

hence $\gamma = 1$.

2. Shockley-Read-Hall recombination

The compact form of the SRH recombination expression is

$$U_{\mathrm{SRH}} = \frac{(np - n_i^2)}{\tau_n(p + p_t) + \tau_p(n + n_t)}.$$

τ_n and τ_n are the trap electron and hole recombination lifetimes and n_t and p_t are the electron and hole densities when the Fermi level is at the trap level, E_t, for example, for electrons

$$n_t = n_i \exp\left(\frac{E_t - E_{\mathrm{CB}}}{k_B T}\right),$$

where E_{CB} is the conduction-band energy.

3. Shallow traps, $n = p$

For shallow traps close to the conduction-band, in most cases, $E_{Fn} < E_t$ and $n \ll n_t$, $p \gg p_t$ and $p \ll n_t$. Where $n = p$, the rate of recombination is determined by both charge-carrier densities

$$U_{\mathrm{SRH}} \approx \frac{np}{\tau_n p + \tau_p n_t} \approx \frac{n^2}{\tau_p n_t},$$

hence $\gamma = 2$.

4. Midband-gap traps, $n = p$

For deep traps where, in the presence of a bias $E_{Fn} > E_t$, as a result $n \gg n_t$ and $p \gg p_t$. If $n = p$ then

$$U_{\mathrm{SRH}} \approx \frac{np}{\tau_n p + \tau_p n} = \frac{n^2}{n(\tau_n + \tau_p)} = \frac{n}{(\tau_n + \tau_p)},$$

hence $\gamma = 1$.

5. Shallow traps, $n \gg p$

For shallow traps close to the conduction-band, in most cases, $E_{Fn} < E_t$ and $n \ll n_t$, $p \gg p_t$ and $p \ll n_t$. If $n \gg p$ and n are approximately constant (for example, if n is pinned by the contact concentration n_{contact}), then recombination is limited by the availability of holes

$$U_{\mathrm{SRH}} \approx \frac{np}{\tau_n p + \tau_p n_t} \approx \frac{n_{\mathrm{contact}} p}{\tau_p n_t},$$

hence $\gamma = 1$. However, this does not necessarily hold in general. In the cases considered in the main text, this implies that the above approximation will be valid following forward-bias preconditioning, but not zero- or reverse-bias preconditioning.

6. Midband-gap traps, $n \gg p$

For deep traps in the presence of a bias where $E_{Fn} > E_t$, then $n \gg n_t$ and $p \gg p_t$. In a situation where $n \gg p$, recombination is limited by the availability of holes

$$U_{\mathrm{SRH}} \approx \frac{np}{\tau_n p + \tau_p n} \approx \frac{np}{\tau_p n} \approx \frac{p}{\tau_p},$$

hence $\gamma = 1$.

APPENDIX C: DEVICE SIMULATION PARAMETER SETS

Table IV gives the core device parameters used in the p-i-n drift diffusion simulation. Further details of the simulation can be found in Ref. [8].

TABLE IV. Key simulation device parameters.

Parameter name	Symbol	Value	Unit	Ref.
Band gap	E_g	1.6	eV	[50]
Built-in voltage	V_{BI}	1.3	V	[51]
Dielectric constant	ϵ_s	20		[52]
Mobile ionic-defect density	N_{ion}	10^{19}	cm^{-3}	[34]
Ion mobility	μ_a	10^{-12}	cm^2 V^{-1} s^{-1}	
Electron mobility	μ_e	20	cm^2 V^{-1} s^{-1}	[53]
Hole mobility	μ_h	20	cm^2 V^{-1} s^{-1}	[53]
p-type donor density	N_A	3.0×10^{17}	cm^{-3}	
N-type acceptor density	N_D	3.0×10^{17}	cm^{-3}	
Effective density of states	N_0	10^{20}	cm^{-3}	[9]

APPENDIX D: RECOMBINATION SCHEME PARAMETERS

The following tables give the specific device recombination parameters used in the simulation for each of the tested recombination schemes. Trap energies are referenced to the electron affinity of the material.

1. Band-to-band recombination

Parameter	p-type	Intrinsic	n-type	Unit
k_{BTB}	10^{-10}	10^{-10}	10^{-10}	cm^3 s^{-1}
τ_n	...	...	...	s
τ_p	...	...	...	s
E_t	...	...	...	eV

2. Interfacial SRH, shallow traps

Parameter	p-type	Intrinsic	n-type	Unit
k_{BTB}	10^{-10}	10^{-10}	10^{-10}	cm^3 s^{-1}
τ_n	10^{-15}	...	10^{-15}	s
τ_p	10^{-15}	...	10^{-15}	s
E_t	-1.4	...	-0.2	eV

3. Interfacial SRH, midgap traps

Parameter	p-type	Intrinsic	n-type	Unit
k_{BTB}	10^{-10}	10^{-10}	10^{-10}	cm^3 s^{-1}
τ_n	10^{-10}	...	10^{-12}	s
τ_p	10^{-10}	...	10^{-12}	s
E_t	-0.8	...	-0.8	eV

4. Bulk SRH, shallow traps

Parameter	p-type	Intrinsic	n-type	Unit
k_{BTB}	10^{-10}	10^{-10}	10^{-10}	cm^3 s^{-1}
τ_n	...	10^{-15}	...	s
τ_p	...	10^{-15}	...	s
E_t	...	-0.2	...	eV

5. Bulk SRH, midgap traps

Parameter	p-type	Intrinsic	n-type	Unit
k_{BTB}	10^{-10}	10^{-10}	10^{-10}	cm^3 s^{-1}
τ_n	...	10^{-10}	...	s
τ_p	...	10^{-10}	...	s
E_t	...	-0.8	...	eV

While the nominal band-to-band rate coefficients are set reasonably high, it can be shown that SRH recombination would still dominate in all cases provided that $\tau_{SRH} \ll k_{BTB} n$. We start by expressing recombination U as a sum of SRH and band-to-band recombination

$$U = \frac{1}{\tau_{SRH}} n + k_{BTB} n^2.$$

If SRH dominates

$$\frac{1}{\tau_{SRH}} n \gg k_{BTB} n^2.$$

This leads to the condition

$$n \ll \frac{1}{\tau_{SRH} k_{BTB}}.$$

Hence, where $\tau_{SRH} = k_{BTB} = 10^{-10}$ as in scheme 5, provided $n < 10^{20}$ cm^{-3}, which is guaranteed by the choice of 10^{20} cm^{-3} for the effective density of states, SRH will dominate.

APPENDIX E: DISCREPANCIES BETWEEN $N_{id}(T \approx 0)$ FOR $V_{pre} = 0$ DERIVED FROM Suns-V_{OC} AND Suns-PL MEASUREMENTS

For the mp-TiO$_2$ cell, although the changes in n_{id} values from Suns-PL and Suns-V_{OC} are consistent as V_{pre} is varied, the absolute values of n_{id} for $V_{pre} = 0$ are lower with the Suns-PL measurements [$n_{id}(t \approx 0) = 1.8$] than the corresponding Suns-V_{OC} measurements [$n_{id}(t \approx 0) = 3.2$]. This difference in absolute values may be related to the relatively localized generation of charge carriers by the laser spot during the Suns-PL measurement, which might avoid localized recombination shunts (dependent on the ion distribution). These shunts would not be avoided during the Suns-V_{OC} measurements since charge carriers are generated over the whole cell area.

APPENDIX F: DEVICE-TO-DEVICE VARIABILITY IN THE TRANSIENT IDEALITY FACTOR

A significant issue for perovskite solar cells is variation in the properties of devices nominally prepared by the same methods. This issue has been noted by many authors including Pockett *et al.* who observed significant differences in the steady-state ideality factor observed for devices prepared in an identical way [13]. We also observe a similar phenomenon, with differences in the initial ideality factor values as well as at steady state. For example, for a batch of six planar compact TiO$_2$ cells manufactured in a different laboratory from those described above, initial idealities after forward biasing at $V_{pre} = 1.1$ V are $0.97 < n_{id}(t \approx 0) < 4.22$ ($\bar{n}_{id}(t \approx 0) = 1.78$, $\sigma_{nid} = 1.16$), while for mp-TiO$_2$ architectures following the same preconditioning, the values are $0.04 < n_{id}(t \approx 0) < 1.12$ ($\bar{n}_{id}(t \approx 0) = 0.75$, $\sigma_{nid} = 0.62$,

for six devices). Mesoporous TiO_2 devices with triple-cation active layers show greater consistency with initial idealities after forward biasing of $0.40 < n_{id}(t \approx 0) < 1.04$ [$\bar{n}_{id}(t \approx 0) = 0.77$, $\sigma_{n_{id}} = 0.32$, for three devices]. The values close to 1 here might suggest that recombination at the compact TiO_2 layer interface is more significant than at the mp-TiO_2/$CH_3NH_3PbI_3$ interface in these devices. However, the unexpectedly high n_{id} and standard deviation suggest that the recombination kinetics at any given interface type are highly dependent on localized details of the interface formation during device fabrication. Degradation during measurements could account for particularly low ideality factors since the V_{OC} transients are measured in order of intensity from lowest to highest. If degradation is continuous throughout the measurement, V_{OC} would be lower than expected at higher light intensity, reducing the measured n_{id}. Further work on high-performing, stable devices will be required to more confidently ascertain whether or not the signature transient idealities presented in this study allow more general statements on identifying the dominant recombination mechanism in different perovskite device architectures and material combinations.

APPENDIX G: TRANSIENT SYSTEM TECHNICAL SPECIFICATIONS

Data-acquisition is performed by a Tektronix DPO5104B digital oscilloscope and a National Instruments USB-6361 DAQ. The laser pulse is provided by a digitally modulated Omicron PhoxX + 638-nm-diode laser with a 100-Hz repetition rate. The laser spot size is expanded to cover the active pixel and the continuous-wave intensity over the cell pixel area is approximately 550 mW cm^{-2} during the pulse. The preconditioning bias is applied using the data-acquisition card and the system is controlled by a custom Labview code. See Fig. 8.

APPENDIX H: OPTICAL MODELING OF DEVICES WITH TRANSPARENT CONDUCTIVE ADHESIVE ELECTRODE

The normalized optical power density is modeled for a mp-TiO_2 device stack with a TCA top electrode using a simple Beer-Lambert function such that the light intensity φ at position x in each layer falls exponentially in each layer

$$\phi(x) = \phi_0 \exp(-\alpha x),$$

where φ_0 is the intensity at the start of the layer and α is the absorption coefficient of the material. For the mp-TiO_2, the optical constants are calculated using the values for pure perovskite and TiO_2 phases in proportions of 1:1 by volume fraction. The polyethylene terephthalate (PET) layer of the TCA is assumed to be completely transparent.
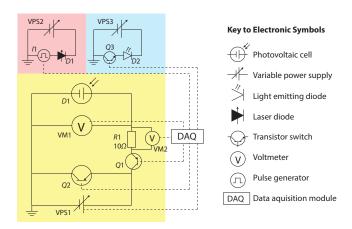

FIG. 8. Transient optoelectronic measurement system circuit diagram. Circuit diagram for the transient data-acquisition system. The yellow shaded area is the primary circuit, which allows the cell to be electrically biased and switched between open and closed circuits. The light red shaded area is the laser circuit and the light blue shaded region is the white bias light-emitting diode (LED) circuit. Figure reproduced from Ref. [8] (Creative Commons license).
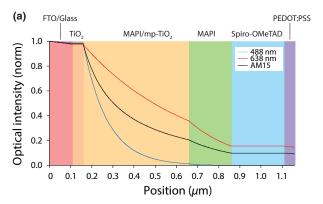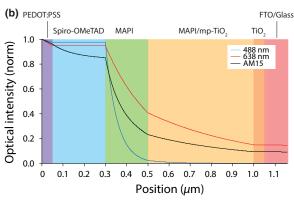

FIG. 9. Optical modeling of the mp-TiO_2 device with TCA electrode used in the transient photovoltage measurements. Optical intensity as a function of position for the mp-TiO_2 device stack incorporating the TCA electrode. Illumination from (a) the FTO-glass side and (b) the TCA side. Blue and red curves indicate wavelengths of 488 nm and 638 nm respectively, while the black curve shows the decay of the AM1.5 spectrum integrated from 300 to 768 nm.

The optical constants are obtained from Refs. [50,54]. See Fig. 9.

---

[1] C. T. Sah, R. N. Noyce, and W. Shockley, Carrier generation and recombination in P-N Junctions and P-N junction characteristics, Proc. IRE **45,** 1228 (1957).

[2] L. J. Koster, V. D. Mihailetchi, R. Ramaker, and P. W. Blom, Light intensity dependence of open-circuit voltage of polymer:fullerene solar cells, Appl. Phys. Lett. **86,** 123509 (2005).

[3] T. Kirchartz, F. Deledalle, P. S. Tuladhar, J. R. Durrant, and J. Nelson, On the differences Between dark and light ideality factor in polymer:fullerene solar cells, J. Phys. Chem. Lett. **4,** 2371 (2013).

[4] A. Pockett and M. J. Carnie, Ionic influences on recombination in perovskite solar cells, ACS Energy Lett. **2,** 1683 (2017).

[5] Davide Moia, Ilario Gelmetti, Philip Calado, William Fisher, Michael Stringer, Onkar S. Game, Yinghong Hu, Pablo Docampo, David George Lidzey, Emilio J. Palomares, Jenny Nelson, and Piers R. F. Barnes, Ionic-to-electronic current amplification in hybrid perovskite solar cells: ionically gated transistor-interface circuit model explains hysteresis and impedance of mixed conducting devices, Energy Environ. Sci. Accepted manuscript (2019).

[6] M. T. Neukom, S. Züfle, E. Knapp, M. Makha, R. Hany, and B. Ruhstaller, Why perovskite solar cells with high efficiency show small IV-curve hysteresis, Sol. Energy Mater. Sol. Cells **169,** 159 (2017).

[7] D. A. Jacobs, H. Shen, F. Pfeffer, J. Peng, T. P. White, F. J. Beck, and K. R. Catchpole, The two faces of capacitance: New interpretations for electrical impedance measurements of perovskite solar cells and their relation to hysteresis, J. Appl. Phys. **124,** 225702 (2018).

[8] P. Calado, A. M. Telford, D. Bryant, X. Li, J. Nelson, B. C. O'Regan, and P. R. F. Barnes, Evidence for ion migration in hybrid perovskite solar cells with minimal hysteresis, Nat. Commun. **7,** 13831 (2016).

[9] S. van Reenen, M. Kemerink, and H. J. Snaith, Modeling anomalous hysteresis in perovskite solar cells, J. Phys. Chem. Lett. **6,** 3808 (2015).

[10] R. A. Belisle, W. H. Nguyen, A. R. Bowring, P. Calado, X. Li, S. J. C. Irvine, M. D. Mcgehee, P. R. F. Barnes, and B. C. O'Regan, Interpretation of inverted photocurrent transients in organic lead halide perovskite solar cells: Proof of the field screening by mobile ions and determination of the space charge layer widths, Energy Environ. Sci. **10,** 192 (2016).

[11] B. C. O'Regan, P. R. F. Barnes, X. Li, C. Law, E. Palomares, and J. M. Marin-Beloqui, Opto-electronic studies of methylammonium lead iodide perovskite solar cells with mesoporous TiO2: Separation of electronic and chemical charge storage, understanding two recombination lifetimes, and the evolution of band offsets during JV hysteresis, J. Am. Chem. Soc. **137,** 5087 (2015).

[12] W. Tress, N. Marinova, T. Moehl, S. M. Zakeeruddin, M. K. Nazeeruddin, and M. Grätzel, Understanding the rate-dependent J–V hysteresis, slow time component, and

aging in $CH_3NH_3PbI_3$ perovskite solar cells: The role of a compensated electric field, Energy Environ. Sci. **8,** 995 (2015).

[13] A. Pockett, G. E. Eperon, T. Peltola, H. J. Snaith, A. Walker, L. M. Peter, and P. J. Cameron, Characterization of planar lead halide perovskite solar cells by impedance spectroscopy, open-circuit photovoltage decay, and intensity-modulated photovoltage/photocurrent spectroscopy, J. Phys. Chem. C **119,** 3456 (2015).

[14] W. Tress, M. Yavari, K. Domanski, P. K. Yadav, B. Niesen, J. P. Correa-Baena, A. Hagfeldt, and M. Grätzel, Interpretation and evolution of open-circuit voltage, recombination, ideality factor and subgap defect states during reversible light-soaking and irreversible degradation of perovskite solar cells, Energy Environ. Sci. **11,** 151 (2017).

[15] T. Leijtens, A. R. Srimath Kandada, G. E. Eperon, G. Grancini, V. D'Innocenzo, J. M. Ball, S. D. Stranks, H. J. Snaith, and A. Petrozza, Modulating the electron-hole interaction in a hybrid lead halide perovskite with an electric field, J. Am. Chem. Soc. **137,** 15451 (2015).

[16] Y. Zhao, W. Zhou, W. Ma, S. Meng, H. Li, J. Wei, R. Fu, K. Liu, D. Yu, and Q. Zhao, Correlations between immobilizing ions and suppressing hysteresis in perovskite solar cells, ACS Energy Lett. **1,** 266 (2016).

[17] V. Sarritzu, N. Sestu, D. Marongiu, X. Chang, S. Masi, A. Rizzo, S. Colella, F. Quochi, M. Saba, A. Mura, and G. Bongiovanni, Optical determination of shockley-read-hall and interface recombination currents in hybrid perovskites, Sci. Rep. **7,** 44629 (2017).

[18] P. Calado, P. R. F. Barnes, I. Gelmetti, M. Azzouzi, and B. Hilton, Driftfusion, (2017). Available at: https://github.com/barnesgroupICL/Driftfusion.

[19] S. Agarwal, M. Seetharaman, N. K. Kumawat, A. S. Subbiah, S. K. Sarkar, D. Kabra, M. A. G. Namboothiry, and P. R. Nair, On the uniqueness of ideality factor and voltage exponent of perovskite-based solar cells, J. Phys. Chem. Lett. **5,** 4115 (2014).

[20] J. P. Correa-Baena, W. Tress, K. Domanski, E. H. Anaraki, S. H. Tureen-Cruz, B. Roose, P. P. Boix, M. Gra, and A. Hagfeldt, Identifying and suppressing interfacial recombination to achieve high open-circuit voltage in perovskite solar cells, Energy Environ. Sci. **10,** 1207 (2017).

[21] G. A. H. Wetzelaer, M. Kuik, M. Lenes, and P. W. M. Blom, Origin of the dark-current ideality factor in polymer:fullerene bulk heterojunction solar cells, Appl. Phys. Lett. **99,** 153506 (2011).

[22] T. Kirchartz and J. Nelson, Meaning of reaction orders in polymer:fullerene solar cells, Phys. Rev. B **86,** 165201 (2012).

[23] W. Shockley and W. T. Read, Statistics of the recombination of holes and electrons, Phys. Rev. **87,** 835 (1952).

[24] J. Xu, A. Buin, A. H. Ip, W. Li, O. Voznyy, R. Comin, M. Yuan, S. Jeon, Z. Ning, J. J. McDowell, P. Kanjanaboos, J. P. Sun, X. Lan, L. N. Quan, D. H. Kim, I. G. Hill, P. Maksymovych, and E. H. Sargent, Perovskite–fullerene hybrid materials suppress hysteresis in planar diodes, Nat. Commun. **6,** 7081 (2015).

[25] K. Wojciechowski, S. D. Stranks, A. Abate, G. Sadoughi, A. Sadhanala, N. Kopidakis, G. Rumbles, C. Li, R. H. Friend, A. K. Jen, and H. J. Snaith, Heterojunction modification for highly efficient organic-inorganic

perovskite solar cells, ACS Nano **8,** 12701 (2014).

[26] A. Foertig, J. Rauh, V. Dyakonov, and C. Deibel, Shockley equation parameters of P3HT:PCBM solar cells determined by transient techniques, Phys. Rev. B **86,** 115302 (2012).

[27] T. Kirchartz, B. E. Pieters, J. Kirkpatrick, U. Rau, and J. Nelson, Recombination via tail states in polythiophene: fullerene solar cells, Phys. Rev. B **83,** 115209 (2011).

[28] O. Breitenstein, P. Altermatt, K. Ramspeck, and A. Schenk, in *21st Eur. Photovolt. Sol. Energy Conf. WIP* (2006), p. 625.

[29] M. M. Lee, J. Teuscher, T. Miyasaka, T. N. Murakami, and H. J. Snaith, Efficient hybrid solar cells based on meso-superstructured organometal halide perovskites, Science **338,** 643 (2012).

[30] H. S. Kim, C. R. Lee, J. H. Im, K. B. Lee, T. Moehl, A. Marchioro, S. J. Moon, R. Humphry-Baker, J. H. Yum, J. E. Moser, M. Grätzel, and N. G. Park, Lead iodide perovskite sensitized all-solid-state submicron thin film mesoscopic solar cell with efficiency exceeding 9%, Sci. Rep. **2,** 591 (2012).

[31] P. R. F. Barnes, K. Miettunen, X. Li, A. Y. Anderson, T. Bessho, M. Gratzel, and B. C. O'Regan, Interpretation of optoelectronic transient and charge extraction measurements in dye-sensitized solar cells, Adv. Mater. **25,** 1881 (2013).

[32] See Supplemental Material at http://link.aps.org/supple mental/10.1103/PhysRevApplied.11.044005 for additional data, schematics and figures.

[33] A. Walsh, D. O. Scanlon, S. Chen, X. G. Gong, and S. Wei, Self-regulation mechanism for charged point defects in hybrid, Angew. Chemie Int. Ed. **54,** 1791 (2015).

[34] C. Eames, J. M. Frost, P. R. F. Barnes, B. C. O'Regan, A. Walsh, and M. S. Islam, Ionic transport in hybrid lead iodide perovskite solar cells, Nat. Commun. **6,** 7497 (2015).

[35] J. M. Azpiroz, E. Mosconi, J. Bisquert, and F. De Angelis, Defect migration in methylammonium lead iodide and its role in perovskite solar cell operation, Energy Environ. Sci. **8,** 2118 (2015).

[36] J. Haruyama, K. Sodeyama, L. Han, and Y. Tateyama, First-principles study of ion diffusion in perovskite solar cell sensitizers, J. Am. Chem. Soc. **137,** 10048 (2015).

[37] S. Meloni, T. Moehl, W. Tress, M. Franckevičius, M. Saliba, Y. H. Lee, P. Gao, M. K. Nazeeruddin, S. M. Zakeeruddin, U. Rothlisberger, and M. Graetzel, Ionic polarization-induced current-voltage hysteresis in $CH_3NH_3PbX_3$ perovskite solar cells, Nat. Commun. **7,** 10334 (2016).

[38] T. Zhang, H. Chen, Y. Bai, S. Xiao, L. Zhu, C. Hu, Q. Xue, and S. Yang, Understanding the relationship between ion migration and the anomalous hysteresis in high-efficiency perovskite solar cells: A fresh perspective from halide substitution, Nano Energy **26,** 620 (2016).

[39] W. J. Yin, T. Shi, and Y. Yan, Unusual defect physics in $CH_3NH_3PbI_3$ perovskite solar cell absorber, Appl. Phys. Lett. **104,** 063903 (2014).

[40] M. Du, Density functional calculations of native defects in $CH_3NH_3PbI_3$: Effects of spin-orbit coupling and self-interaction error, J. Phys. Chem. Lett. **6,** 1461 (2015).

[41] https://github.com/barnesgroupICL/Driftfusion.

[42] J. Yao, T. Kirchartz, M. S. Vezie, M. A. Faist, W. Gong, Z. He, H. Wu, J. Troughton, T. Watson, D. Bryant, and J. Nelson, Quantifying Losses in Open-Circuit Voltage in Solution-Processable Solar Cells, Phys. Rev. Appl. **4,** 014020 (2015).

[43] B. C. O'Regan, J. R. Durrant, P. M. Sommeling, and N. J. Bakker, Influence of the $TiCl_4$ treatment on nanocrystalline TiO_2 films in dye-sensitized solar cells. 2. Charge density, band edge shifts, and quantification of recombination losses at short circuit, J. Phys. Chem. C **111,** 14001 (2007).

[44] P. Docampo, S. Guldin, M. Stefik, P. Tiwana, M. C. Orilall, S. Hüttner, H. Sai, U. Wiesner, U. Steiner, and H. J. Snaith, Control of solid-state dye-sensitized solar cell performance by block-copolymer-directed TiO_2 synthesis, Adv. Funct. Mater. **20,** 1787 (2010).

[45] D. Bryant, P. Greenwood, J. Troughton, M. Wijdekop, M. Carnie, M. Davies, K. Wojciechowski, H. Snaith, T. Watson, and D. Worsley, A transparent conductive adhesive laminate electrode for high efficiency organic-inorganic lead halide perovskite solar cells, Adv. Mater. **26,** 7499 (2014).

[46] J. Shi, X. Xu, H. Zhang, Y. Luo, D. Li, and Q. Meng, Intrinsic slow charge response in the perovskite solar cells: Electron and ion transport, Appl. Phys. Lett. **107,** 163901 (2015).

[47] M. Neukom, S. Züfle, S. Jenatsch, and B. Ruhstaller, Opto-electronic characterization of third-generation solar cells, Sci. Technol. Adv. Mater. **19,** 291 (2018).

[48] W. Tress, K. Leo, and M. Riede, Influence of hole-transport layers and donor materials on open-circuit voltage and shape of I-V curves of organic solar cells, Adv. Funct. Mater. **21,** 2140 (2011).

[49] K. Domanski, B. Roose, T. Matsui, M. Saliba, S. H. Turren-Cruz, J. P. Correa-Baena, C. R. Carmona, G. Richardson, J. M. Foster, F. De Angelis, J. M. Ball, A. Petrozza, N. Mine, M. K. Nazeeruddin, W. Tress, M. Grätzel, U. Steiner, A. Hagfeldt, and A. Abate, Migration of cations induces reversible performance losses over day/night cycling in perovskite solar cells, Energy Environ. Sci. **10,** 604 (2017).

[50] A. M. A. Leguy, P. Azarhoosshm, M. I. Alonso, M. Campoy-quiles, O. J. Weber, J. Yao, D. Bryant, M. T. Weller, J. Nelson, A. Walsh, M. van Schilfgaarde, and P. R. F. Barnes, Experimental and theoretical optical properties of methy-lammonium lead halide perovskites, Nanoscale **8,** 6317 (2016).

[51] P. Schulz, L. L. Whittaker-brooks, B. A. Macleod, D. C. Olson, Y. Loo, and A. Kahn, Electronic level alignment in inverted organometal perovskite solar cells, Adv. Mater. Interfaces **2,** 1400532 (2015).

[52] N. Onoda-Yamamuro, T. Matsuo, and H. Suga, Dielectric study of $CH_3NH_3PbX_3$ (X = Cl, Br, I), J. Phys. Chem. Solids **53,** 935 (1992).

[53] T. Leijtens, S. D. Stranks, G. E. Eperon, R. Lindblad, E. M. J. Johansson, I. J. Mcpherson, J. M. Ball, M. M. Lee, and H. J. Snaith, electronic properties of meso-superstructured and planar organometal halide perovskite films: charge trapping, photodoping, and carrier mobility, ACS Nano **8,** 7147 (2014).

[54] G. F. Burkhard, E. T. Hoke, and M. D. McGehee, Transfer matrix optical modeling, (2011). Available at: https://web.stanford.edu/group/mcgehee/transfermatrix/.